Role of silicon in the precipitation kinetics of dilute Al-Sc-Er-Zr alloys

Nhon Q. Vo [a,c,*], David C. Dunand [a,c], David N. Seidman [a,b,c]

[a] Department of Materials Science and Engineering, Northwestern University, Evanston, IL 60208, USA
[b] Northwestern University Center for Atom-Probe Tomography, Northwestern University, Evanston, IL 60208, USA
[c] NanoAl LLC, Skokie, IL 60077, USA

ARTICLE INFO

ABSTRACT

The precipitate nanostructure and the strength of an Al-0.055Sc-0.005Er-0.02Zr at% alloy with Si additions, in the range 0–0.18 at%, were investigated utilizing micro-hardness, electrical conductivity, scanning electron microscopy and atom-probe tomography techniques. Si-containing alloys are cost-effective due to the existence of Si in commercial purity Al. In all studied alloys, homogenization for at least 0.5 h at 640 °C is needed to eliminate Al_3Er primary precipitates. Alloys containing the higher Si concentrations achieve higher microhardness by increasing the heterogeneous nucleation current of $(Al, Si)_3$ (Sc, Zr, Er) precipitates. The alloy containing 0.18 at% Si achieves an 60% improvement in peak-microhardness compared to the Si-free alloy, during isothermal aging at 400 °C. Silicon additions reduce the peak-aging time in the temperature range 300–400 °C, indicating that the Er and Sc diffusion kinetics are accelerated. Silicon also enhance the Zr diffusion kinetics, accelerating precipitate growth during aging at 300 °C and precipitate coarsening at 400 °C. Addition of Si modifies the concentration profiles within the nanoprecipitates, enhancing the chemical homogeneity of Sc and Er in their cores, rather than forming Er-enriched-cores/Sc-enriched-shells that we have observed in prior research. Finally, the microhardness of the alloys, containing 0.12 and 0.18 at% Si, only diminishes slightly from the peak values after isothermal aging at 375 °C for about 2000 h, suggesting that the studied alloys can be practically utilized at this operating temperature.

© 2016 Elsevier B.V. All rights reserved.

1. Introduction

The effects of dilute additions of Si on the precipitation kinetics of Al-Sc based alloys are not well established in the archival literature. Most studies of Al-Sc-Si alloys address Si as a regular alloying element (that is, with concentrations exceeding 0.15 at%), rather than as an impurity or a micro-alloying element [1–4]. The Al-Sc-Si phase diagram shows that the α-Al(f.c.c.) solid-solution can be in equilibrium with the $L1_2$-ordered Al_3Sc phase, tetragonal Sc_2AlSi_2 (V-phase), and nearly pure Si [5]. To avoid the formation of the V-phase, which degrades the alloy's microhardness [1,3], the Si concentration needs to be maintained below ~0.2 at% [1,3].

Recent research by Beeri et al. [6] demonstrates faster precipitation kinetics and a higher precipitate number density, N_v, from the addition of a trace concentration of Si (~0.025 at%) to dilute binary Al-Sc alloys. This observation is consistent with numerous prior studies concerning a similar effect of Si in Al-TM (TM = transition metal) binary alloys, such as Al-Ti [7], Al-Zr [8–10], Al-Cu [11,12], and Al-Hf [13]. It is believed that an attractive binding energy between Si atoms and vacancies exists, so the Si-vacancy

clusters that form act as heterogeneous nucleation sites for precipitates [14,15]. This explanation is consistent with first-principles calculations and atom-probe tomography (APT) results demonstrating the coexistence of Si and Sc within Al_3Sc precipitates [16].

Another possible explanation is that the enhancement of the precipitate number density is due to a decrease in Sc solubility in the presence of Si in the α-Al matrix, thereby increasing the chemical driving force for precipitation and decreasing the critical net reversible work to form a critical nucleus [2,17]. The Si addition may also reduce the α-Al/Al_3Sc interfacial free energy by segregating at this interface, thereby reducing the critical radius for homogeneous nucleation. These explanations are based, however, on the assumption of homogeneous nucleation, which is rarely observed in nature, especially in multi-element alloys [18]. Furthermore, the nanostructure of Al_3Sc precipitates, as revealed by APT, exhibits the co-precipitation of Si and Sc rather than interfacial segregation of Si at the α-Al/Al_3Sc interface [16].

A recent study combining APT and first-principles calculations explains the role of Si in accelerating precipitation kinetics in an Al-0.06Sc-0.06Zr at% alloy [19]. A strong increase in precipitate number density is observed upon addition 0.06 Si at% to this alloy, after aging at 300 °C for 1 h [19]. First-principles calculations also indicate a strong Si-Sc and Si-Si attractive binding energy at the first

Table 1
Composition (at%) of the studied alloys, as measured by direct current plasma mass spectroscopy (DCPMS) and local-electrode atom-probe (LEAP) tomography. Measurement uncertainty is given in parenthesis after the significant digit to which it applies.

Nominal	Measured alloy composition (DCPMS)				Measured alloy composition (LEAP)			
	Si	Sc	Zr	Er	Si[*]	Sc	Zr	Er
Al-0.05Sc-0.01Er-0.06Zr [21]	< 0.005	0.047	0.035	0.010	< 0.002	0.0476(8)	0.0198(7)	0.0038(4)
Al-0.055Sc-0.005Er-0.02Zr-0.05Si [20]	0.044	0.056	0.021	0.007	0.0401(6)	0.0530(7)	0.0143(4)	0.0039(2)
Al-0.055Sc-0.005Er-0.02Zr-0.12Si	0.125	0.053	0.028	0.004	–	–	–	–
Al-0.055Sc-0.005Er-0.02Zr-0.18Si	0.192	0.055	0.028	0.004	0.1224(7)	0.0583(5)	0.0314(4)	0.0055(2)

[*] Atomic concentration of $^{28}Si^{2+}$ ions in LEAP.

and second nearest-neighbor distances within the precipitates, as well as an attractive binding energy for Si-Sc and Si-Si atomic pairs in the α-Al (f.c.c.) matrix [19]. Additionally, the Sc-vacancy binding energy is reduced by the existence of Si in the α-Al-matrix and the Sc migration energy is reduced from 0.74 eV atom^{-1} in the absence of Si, to 0.45 eV atom^{-1} in the presence of Si [19]. The first-principles calculations provide strong evidence for the role of Si in the experimentally observed acceleration of Al$_3$Sc precipitation kinetics.

Herein, we systematically investigate experimentally the role of Si in precipitation kinetics of an Al-0.055Sc-0.005Er-0.02Zr at% alloy. We previously studied this alloy [20–22] and found the following results: (i) a coarse grain structure advantageous for creep resistance [20]; (ii) good ambient temperature strength due to a high number density of nano-size Al$_3$(Sc, Zr, Er) precipitates [20–22]; (iii) excellent coarsening resistance at 400 °C (a homologous temperature of 0.72 for aluminum), due to formation of a Zr-enriched precipitate shell enveloping the precipitates and therefore forming a diffusion barrier [20,21,23,24]; (iv) excellent high-temperature creep resistance due to formation of an Er-enriched precipitate core, which enhances the precipitates' lattice parameter mismatch with the α-Al matrix, and thereby increasing their elastic interactions with dislocations [22,25–28]; and (v) cost-effectiveness, due to the use of small concentrations of the expensive Sc, and Er and Zr elements. Si additions (< 0.2 at%) provide the following advantages [19]: (i) increasing precipitate number density by inducing a heterogeneous nucleation current; (ii) accelerating the precipitation kinetics of Er and Sc precipitation, which decreases the heat treatment time; and (iii) decreasing the alloy cost because commercial grade aluminum with Si impurities can be used as feedstock.

In the present article, the precipitation kinetics of Al-0.055Sc-0.005Er-0.02Zr at% with the addition of Si concentrations of 0.12 or 0.18 at% are investigated utilizing micro-hardness, electrical conductivity, and APT techniques. The results are compared to a similar alloy without Si and with a low Si concentration of 0.05 at%. Si concentrations greater than 0.18 at% are not studied, to guarantee that V-phase formation does not occur [1,3]. We demonstrate that the alloys containing higher Si concentrations achieve higher precipitate number densities, and thus improved ambient peak-microhardness values. Additionally, we demonstrate that the presence of Si decreases the time to achieve peak strength of the alloy, most probably by accelerating the diffusion kinetics of Er and Sc. Silicon also appears to enhance the diffusion kinetics of Zr as it produces: (i) faster segregation of Zr atoms at the interface of the growing (Al, Si)$_3$(Sc, Er) precipitates during aging at 300 °C; and (ii) an increased coarsening rate of the (Al, Si)$_3$(Sc, Zr, Er) precipitates during aging at 400 °C. Finally, we demonstrate that the precipitates' concentration profiles are strongly modified by the addition of Si when compared to the Si-free alloy.

2. Experimental procedures

Two alloys with a nominal base composition of Al-0.055Sc-0.005Er-0.02Zr at% (Al-0.092Sc-0.031Er-0.068Zr wt%), and concentrations of Si of 0.12 or 0.18 at% (0.12 or 0.19 wt%) referred to as Si12 and Si18, respectively, were melted in alumina crucibles in a resistively heated furnace by adding to molten 99.999 at% pure Al appropriate amounts of Al-12Si at%, Al-5.0Zr at%, Al-1.3Sc at%, Al-1.2Er at% master alloys, which were preheated to 640 °C to accelerate their dissolution during melting. The alloyed melt was maintained in air for 30 min at 800 °C, vigorously stirred, and then cast into a graphite mold. The mold was preheated to 200 °C and placed on an ice-cooled copper platen just before casting to enhance directional solidification. Chemical compositions of all as-cast alloys, which were sampled at different positions in the ingot, were measured by direct current plasma mass spectroscopy (DCPMS) at ATI Wah Chang (Albany, OR), and the results are presented in Table 1. APT was also utilized to measure alloy chemical composition, using the average values of at least two specimens, see Table 1. Prior results from the same alloy without Si [21], referred to as Si00, and with a low Si concentration of 0.05 at% [20], referred to as Si05, are also presented for comparison.

All alloys were homogenized in air at 640 °C for different times, ranging from 5 min to 72 h, and terminated by water quenching. Isothermal aging was performed in air at 300, 375 or 400 °C for times up to 125 days. All heat treatments were performed in air and terminated by water quenching to ambient temperature.

Vickers microhardness measurements were performed with a Duramin-5 microhardness tester (Struers) utilizing an applied load of 200 g for 5 s on samples polished to a 1 μm surface finish. Different applied times did not alter the measurement values. More than ten indentations, through various grains, were made for each specimen to improve the statistics. Electrical conductivity measurements were performed on the mounted samples utilizing a Sigmatest 2.069 eddy current instrument (Foerster Instruments, Pittsburgh, PA). Five measurements were made at the frequencies 120, 240, 480, and 960 kHz for each specimen. A Hitachi S-4800-II Scanning A scanning electron microscope (SEM), equipped with an Oxford INCAx-act detector for energy-dispersive x-ray spectroscopy (EDS) measurements, were utilized for detecting large primary precipitates.

Specimens for three-dimensional (3-D) local-electrode atom-probe (LEAP) tomography were prepared by cutting the alloy with a diamond saw to $\sim 0.4 \times 0.4 \times 10$ mm^3 blanks, which were electropolished at 20–25 Vdc using a solution of 10% perchloric acid in acetic acid, followed by electropolishing at 12–18 Vdc utilizing a solution of 2% perchloric acid in butoxyethanol, both at room temperature [29,30]. Pulsed-laser atom-probe tomography was performed using a LEAP 4000X Si-X tomograph (Cameca, Madison, WI) [31–33] at a specimen temperature of 30–35 K. Focused picosecond ultraviolet (UV) laser pulses (wavelength=355 nm) with a laser beam waist of < 5 μm at the e^{-2} diameter were employed. A pulse frequency of 500 kHz and a laser energy of 0.080 nJ pulse^{-1} were utilized. LEAP tomographic data were analyzed employing IVAS v3.6.1 (Cameca Instruments). All measurement errors were calculated based on counting statistics and standard error propagation techniques [34].

3. Results

3.1. Homogenization time

The three as-cast alloys, Si05, Si12 and Si18, were homogenized at 640 °C for different times ranging from 0 to 72 h. A plot of electrical conductivity as a function of homogenization time, Fig. 1(a), displays an initial conductivity decrease from the as-cast state values in the first hour of homogenization time, followed by a plateau at $\sim$31.8, $\sim$31.6, and $\sim$31.3 MS m^{-1} for the Si05, Si12, and Si18 alloys, respectively. Scanning electron microscope (SEM) micrographs of the as-cast state of Si05 alloy display a small volume fraction of $\sim$1–10 µm diam. primary precipitates, which are Er-rich, but nearly Sc- and Zr-free, and are identified as Al$_3$Er, as reported previously for similar alloys [21,22]. These precipitates are shown to be nearly completely dissolved after 2 h of homogenization. Representative SEM micrographs of the Si05 alloy in the as-cast and 2 h homogenized states are displayed in Fig. 2(a) and (b), respectively. Therefore, the initial decrease in electrical conductivity, for a short homogenization time, is probably due to the dissolution of Al$_3$Er primary precipitates, since Er in solid-solution scatters electrons more strongly than when they are sequestered in precipitates. Formation of Al$_3$Er primary precipitates in the as-cast state in all alloys was not anticipated, since the Er total concentration (0.005 at%) is one order of magnitude less than its maximum solubility in Al-Er binary alloys (0.046 at%) at 640 ºC [35]. Fig. 1(a) demonstrates that the saturation value of the electrical conductivity increases nearly linearly with the Si concentration present in the alloys, thereby indicating that Si is fully dissolved as expected and its concentration in the alloys is less than its solubility at 640 °C in the Al-Si binary alloy, $\sim$0.3 at% [36].

The Vickers microhardness for alloys aged at 400 °C for 4 h as a function of the prior homogenization time at 640 °C is displayed in Fig. 1(b). For the Si05 [20], Si12, and Si18 alloys, with 349, 455, and
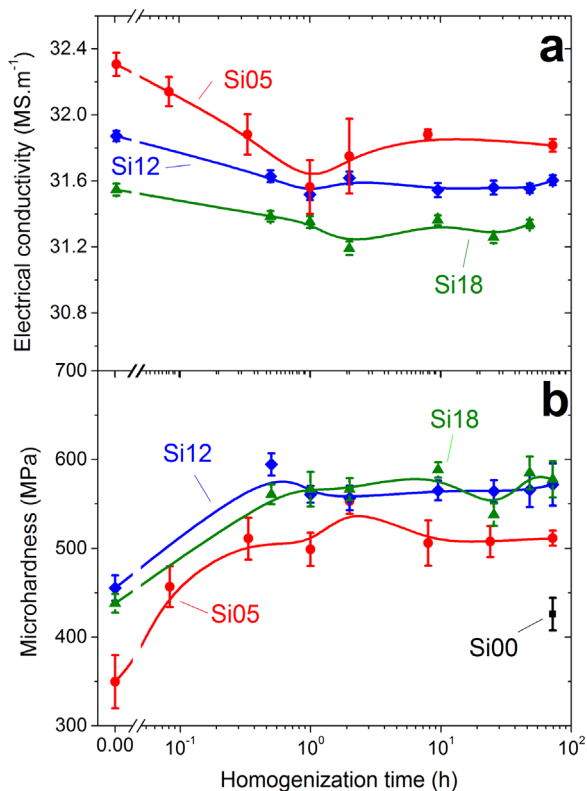

Fig. 2. SEM micrograph of (a) as-cast sample, showing Al$_3$Er primary precipitates, with the inset showing a higher magnification of an Al$_3$Er primary precipitate, and (b) homogenized at 640 °C for 2 h, exhibit no sign of Al$_3$Er primary precipitates in the Si05 alloy.

Fig. 1. Electrical conductivity of the Si05 [20], Si12, and Si18 alloys homogenized at 640 °C for different times (a) and Vickers microhardness of the Si05 [20], Si12, and Si18 alloys homogenized at 640 °C for different times, then aged at 400 °C for 4 h (b).
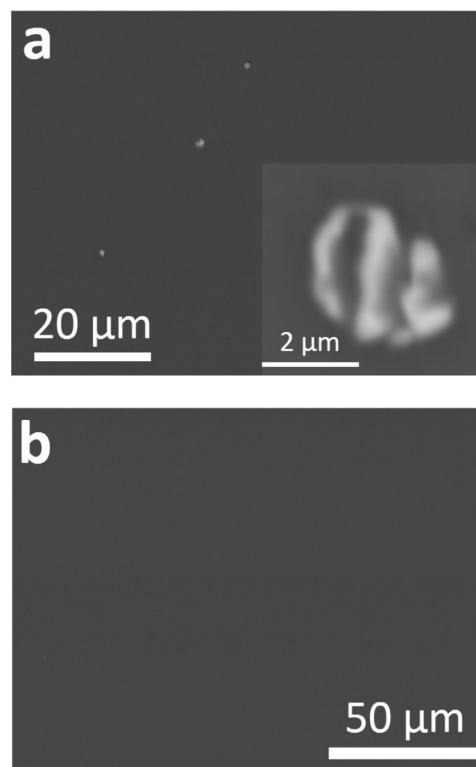
438 MPa initial microhardness values (that is, for alloys that were not homogenized), the microhardness values increase in the first $\sim$0.5 h of homogenization, before saturating at $\sim$520, 565, and 570 MPa, respectively. These trends are similar to the behavior of the electrical conductivity, Fig. 1(a). First, the microhardness increases in the initial 0.5–1 h of homogenization, which is consistent with an increase of the Er concentration in the α-Al matrix due to the dissolution of the Al$_3$Er primary precipitates resulting in solid-solution strengthening, which further enhances the heterogeneous nucleation current and volume fraction of precipitates during aging at 400 °C [21]. Second, the different values of the initial and plateau microhardnesses in Fig. 1(b) can be explained by the effect of Si additions in both the as-cast and homogenized states. In the aged alloys without homogenization (0 h homogenized state, Fig. 1(b)), the microhardnesses of the Si12 and Si18 alloys are similar and $\sim$100 MPa higher than that of the Si05 alloy. Assuming all three alloys have the same Er, Sc, and Zr supersaturations during aging, the higher Si concentration in the α-Al matrix provides additional strengthening, probably by aiding the heterogeneous nucleation of the aged precipitates. In the 72 h homogenized state, where all alloys are anticipated to have the same Er concentrations in the α-Al matrix, the microhardness values of the three alloys decrease with decreasing Si concentration, from a maximum value of 580 $\pm$ 20 MPa for Si12 and Si18 to an intermediate value of 511 $\pm$ 8 MPa for the Si05 alloy, and to a lower value of 426 $\pm$ 18 MPa, for a previously reported, silicon-free Al-0.05Sc-0.01Er-0.06Zr (Si00) alloy [21]: hereafter all concentrations are given in at%, unless otherwise noted. This control Si-free alloy, referred to as Si00, contained $<$ 0.005 at% Si [21]. The α-Al matrix composition, as determined by APT, of this Al-0.05Sc-0.01Er-0.06Zr at% alloy after quenching from the homogenization temperature is much smaller than the nominal alloy composition for Er (0.004 at% Er, a 2.5 fold reduction) and Zr (0.020 at%, a

threefold reduction), due to formation of Al_3Er and Al_3Zr primary precipitates [21], while the Sc concentration is 0.048 at%. The alloy's α-Al matrix composition (Al-0.048Sc-0.004Er-0.020Zr) in which the precipitates form upon aging is, therefore, an essentially Si-free version of the three Si-containing Al-0.055Sc-0.005Er-0.02Zr at% alloys studied herein.

The strength enhancements in the aged alloys, due to micro-additions of Si, are discussed in detail below. Based on these results, all the alloys studied were homogenized for 2 h before any further aging heat treatments.

3.2. Isothermal aging at 300 °C

The temporal evolution of the Vickers microhardnesses and electrical conductivities of all alloys, homogenized for 72 h in the Si00 alloy and 2 h in the Si05 [20], Si12, and Si18 alloys, are plotted as a function of isothermal aging time at 300 °C through 1008 h (42 days) in Fig. 3. For the Si00 alloy, the microhardness increases slightly from 210 ± 7 MPa in the homogenized state to 229 ± 7 MPa after 0.2 h of aging, before rapidly increasing and peaking at 495 ± 19 MPa after 8 h of aging; this value remains constant through the longest aging time of 672 h. All three Si-containing alloys harden faster in the early stage of aging, 0.2–4 h, and exhibit a > 100 MPa increase in microhardness at the longest aging time, as compared to the control Si00 alloy. Their microhardness evolution is similar, within error, except for a slight plateau between 1 and 2 h of aging, which is discussed below. Their microhardness values initially increase at faster rates than the Si00 alloy, from 249 to 281 MPa (typical error bars are 10 MPa) in the homogenized state to 447–507 MPa after 2 h of aging. Then they gradually increase to a plateau of 600–650 MPa achieved after ~140 h and are thereafter constant, within experimental error, through the longest aging time, 1008 h.

As displayed in Fig. 3(b), the electrical conductivity of the Si00 alloy increases gradually from 32.60 ± 0.18 MS m^{-1} in the

homogenized state to 33.93 ± 0.07 MS m^{-1} at the peak-aging time of 8 h, maintaining a constant value of 34.03 ± 0.10 MS m^{-1} between 8 and 168 h; at the longest time of 672 h there is an upward trend. The electrical conductivity and microhardness values suggest that precipitation of the relatively fast diffusers, Er and Sc, is nearly completed after 8 h of aging, resulting in the peak-microhardness values. Precipitation of the very slow diffuser Zr in the α-Al matrix is not occurring, leading to the saturation of the microhardness. The root-mean-square diffusion distance of Zr in pure Al at 300 °C for t=672 h is $\sqrt{4Dt} = 8$ nm, where D is the tracer diffusivity of Zr in Al at that temperature [37]. By contrast, the electrical conductivity of the Si05 alloy increases rapidly initially from 31.82 ± 0.04 MS m^{-1} to 33.62 ± 0.07 MS m^{-1} after 1 h of aging, achieving saturation in the range 1–8 h, before continuously increasing through the longest aging time of 1008 h. The electrical conductivity saturation value, from 1 to 8 h, in the Si05 alloy is comparable to Si00 alloy in the late aging stage, suggesting similar complete precipitation of Er and Sc. The Si05 alloy achieves the electrical conductivity saturation much earlier, however, than in the Si00 alloy indicating an acceleration of the Er and Sc precipitation kinetics. The rapid increase in electrical conductivity beyond 8 h in the Si05 alloy indicates that the slowly diffusing Zr atoms segregate at the interfaces of the existing $Al_3(Er,$ Sc) precipitates, further depleting the α-Al matrix of solute, which causes an increases of the electrical conductivity. The increase in precipitate volume fraction is responsible for the continuously increasing microhardness to the longest aging time of the Si05 alloy. The electrical conductivity evolution of the Si12 alloy is similar to that of the Si05 alloy, but with a barely visible plateau for 2–4 h of aging. The electrical conductivity of the Si18 alloy increases continuously from the homogenized state to the longest aging time of 1008 h, without displaying a plateau. The trend of shorter plateaus as the Si concentration increases is consistent with Si increasing the diffusivity of Zr during diffusion at 300 °C. Similar plateaus for 2–4 h are also discernible in the temporal evolution of the microhardness, Fig. 3(a), which also become shorter with increasing Si concentration.

3.3. Isothermal aging at 400 °C

The temporal evolution of the Vickers microhardness and electrical conductivity of the three Si-containing alloys during isothermal aging at 400 °C through 6,144 h (256 day), after homogenization for 72 h of Si05 alloy [20] and 2 h for the Si12 and Si18 alloys, are displayed in Fig. 4(a) and (b). The microhardness evolution of the Si00 alloy [21], is also plotted, which increases slightly through 0.2 h before increasing significantly to 422 ± 12 MPa at 0.5 h of aging time. It then gradually increases and peaks at 463 ± 20 MPa after 16 day of aging, then diminishes slightly through 256 day of aging due to precipitate coarsening. The microhardness evolution of the Si05 alloy displays several distinct differences compared to the Si00 alloy, Fig. 4. Firstly, the rapid microhardness rise occurs earlier, after only 0.2 h of aging, and a significantly higher microhardness plateau is achieved, ~500 MPa. The microhardness values peak at 533 ± 12 MPa, after 60 h of aging, before diminishing continuously for longer aging times. The microhardness evolution of the Si12 and Si18 alloys are similar. They peak at 571 ± 12 and 607 ± 9 MPa after 2 h of aging, respectively, which is greater and at a much earlier peak-aging time, compared to 16 day for the Si00 alloy [21] and 60 h for the Si05 alloy. They diminish slightly after 169 and 17 h of aging, respectively, after which they decrease more rapidly, reaching 392 ± 11 and 368 ± 9 MPa at the longest aging time of 2,256 h in the Si12 and Si18 alloys, respectively. The rate of microhardness decrease in the Si12 and Si18 alloys is 2- to 3-fold higher than for the Si00 and Si05 alloys at the later stage of aging.

Microhardness values for the four alloys in the homogenized state and for the peak-aging condition at 400 °C, are plotted as a function
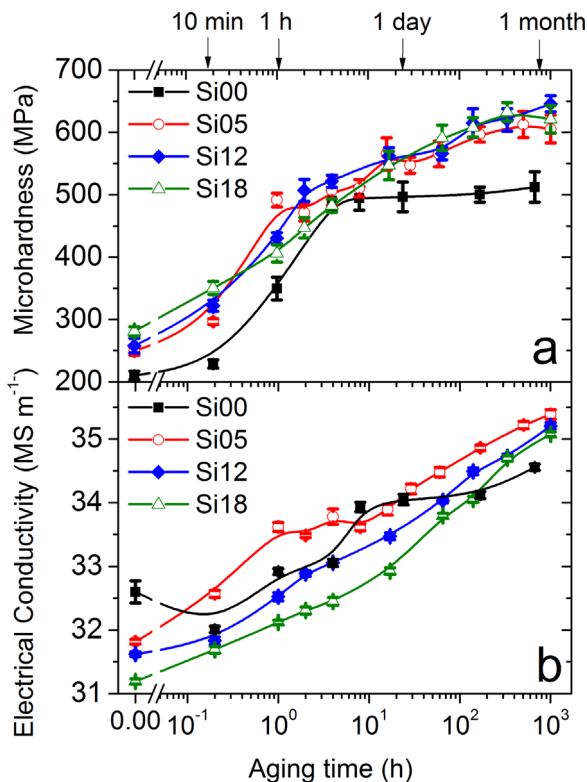

Fig. 3. Evolution of Vickers microhardness and electrical conductivity during isothermal aging at 300 °C, after being homogenized at 640 °C for 72 h in the Si00 [21] and for 2 h in the Si05 [20], Si12, and Si18 alloys.
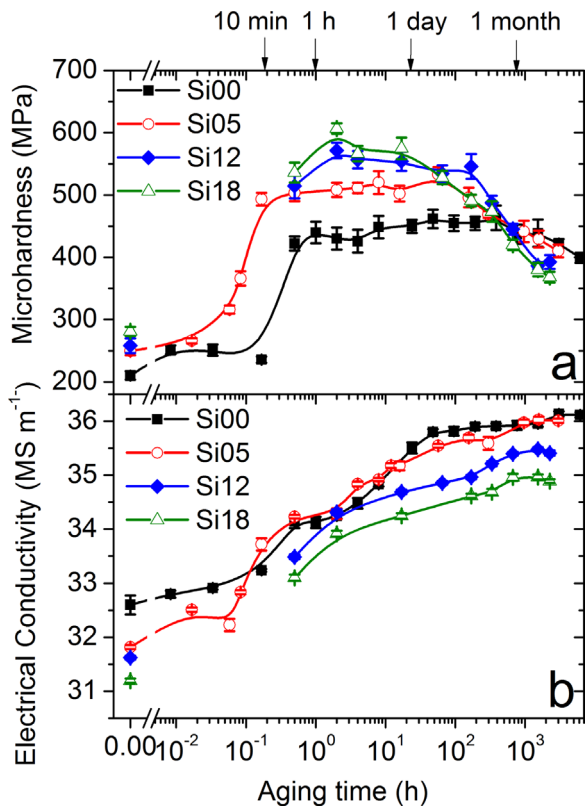
Fig. 4. Evolution of Vickers microhardness and electrical conductivity during isothermal aging at 400 °C after being homogenized at 640 °C for 72 h in the Si00 [21] and Si05 [20], and for 2 h in the Si12 and Si18 alloys.
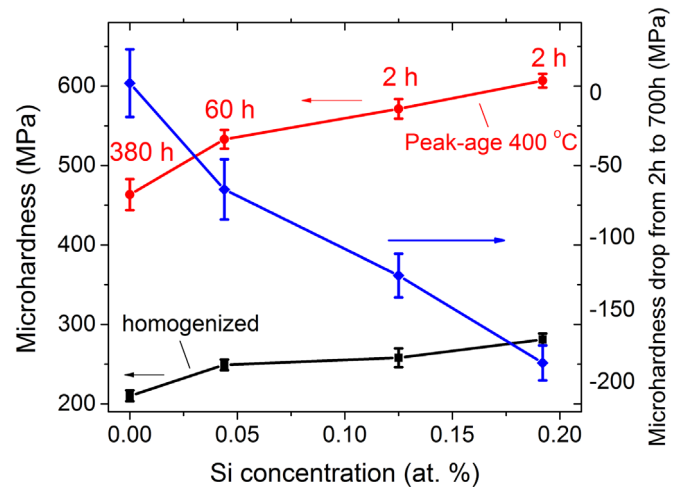

Fig. 5. Microhardness of all studied alloys at the homogenized state and peak-microhardness, aged at 400 °C (Fig. 4) are plotted as a function of Si concentration. Microhardness drop during aging at 400 °C (Fig. 4) from 2 to 700 h is also plotted.

of Si concentration in Fig. 5. The alloy, containing higher Si concentrations, has a higher microhardness in the homogenized state, 210 ± 7, 249 ± 7, 258 ± 12, and 281 ± 7 MPa, achieving a higher peak-microhardness, 463 ± 20, 533 ± 12, 571 ± 12, and 607 ± 9 MPa, and at a shorter aging time, 384, 60, 2, and 2 h in the Si00 [21], Si05 [20], Si12, and Si18 alloy, respectively. The alloy, containing a higher Si concentration exhibits, however, a more rapid decrease in microhardness at the late stage of aging: -7 ± 23, 67 ± 21, 126 ± 15, 187 ± 12 in microhardness decrease, from 2 to 700 h of aging time, in the Si00 [21], Si05 [20], Si12, and Si18 alloy, respectively.

The electrical conductivity of the Si00 alloy [21], Fig. 4(b), increases steadily through 0.5 h of aging, indicating the continuous precipitation of Er and Sc, then saturates from 0.5 to 2 h indicating that the Al$_3$(Er, Sc) precipitates are not growing. Then it increases further through 50 h, indicating that Zr atoms at the matrix/precipitate interface go back into the solution. It saturates at longer aging times as the α-Al matrix evolves toward a thermodynamic equilibrium state and the precipitates coarsen. The electrical conductivity of the Si05 alloy is similar to that of the Si00 alloy, except for an abrupt increase in the range 0.06–0.5 h of aging, coinciding with the rapid increase in microhardness, providing further evidence that the precipitation kinetics of Er and Sc are accelerated by the addition of 0.05 at% Si. The electrical conductivities of the Si12 and Si18 alloys are similar to each other. They rapidly increase from the homogenized state to 2 h of aging, before gradually increasing to the longest aging time of 94 day. A monotonic relationship between the nominal Si concentration and the electrical conductivity values of the alloys exists for alloys aged beyond 1000 h at 400 °C. At this late stage of aging the precipitation of Er, Sc, and Zr is anticipated to be nearly completed, and only Si solute atoms remain in appreciable quantities in the α-Al matrix. Hence, the smaller electrical conductivity (larger resistivity) value of the alloy containing a higher Si concentration is due to the higher Si solubility in the α-Al matrix.

3.4. Isothermal aging at 375 °C

Temporal evolution of the Vickers microhardness and electrical conductivity during aging at 375 °C of the Si00 alloy, after being homogenized for 72 h, and the Si12 and Si18 alloys, after being homogenized for 2 h; Fig. 6(a) and (b). Fig. 6(a) demonstrates that the microhardness of the Si00 alloy is 494 ± 21 MPa after 0.5 h of aging, gradually increases to 563 ± 24 MPa after 168 h of aging, before diminishing slightly at longer aging times, through 86 day. The microhardness of the Si18 alloy peaks at 591 ± 21 MPa after 6 h of aging, reaches saturation from 6 to 360 h, before diminishing slightly at longer aging times up to ∼2000 h. The microhardness of the Si12 alloy achieves a value of 590 ± 12 MPa after 360 h of aging and slightly diminishes through longer times up to ∼2000 h. The electrical conductivity of all three alloys increases steadily with increasing aging time, Fig. 6(b), indicating the continuous precipitation of Er, Sc, and Zr through the longest measured aging time, 86 day.

3.5. Atom-probe tomography

3.5.1. Early stage of isothermal aging at 400 °C

The nanosize precipitates in the Si05 alloy aged isothermally for 0.5 h at 400 °C, after being homogenized for 72 h [20], and in the Si18 alloy aged isothermally for 0.5 and 2 h at 400 °C, after being homogenized at 640 °C for 2 h, are compared utilizing 3-D APT reconstructions [31,32,38] (Fig. 7) and associated concentration profiles, as discussed in detail [39–41], Fig. 8. After 0.5 h of aging, the Si05 alloy exhibits precipitates with a number density of $0.79 \pm 0.22 \times 10^{22}$ m^{-3}, a mean radius of 4.1 ± 0.8 nm, and a volume fraction, ϕ, of 0.235% [20], Table 2. The average precipitate composition, based on seven precipitates, is 73.35 Al, 0.30 Zr, 21.38 Sc, 2.22 Er, and 2.75 Si at%, Table 3. For the same aging time, the Si18 alloy exhibits precipitates with a three-fold higher number density ($2.23 \pm 0.57 \times 10^{22}$ m^{-3}), a ∼35% smaller mean radius (2.9 ± 0.7 nm), and a similar volume fraction (0.229%), Table 2. The average precipitate composition (nine precipitates) is 74.36 Al, 1.41 Zr, 16.72 Sc, 1.54 Er, and 5.81 at% Si, Table 3. The precipitates in both alloys display nearly constant concentration profiles for Sc, Er, and Si, but an enrichment in Zr near the outer surface of the precipitates, Fig. 8; this enrichment becomes more pronounced as the Si concentration of the alloy increases. The following scenario is likely: Sc, Er, and Si co-precipitate during the early stage of aging, while Zr precipitates during the later stages. Formation of a Zr-enriched shell in both alloys (0.5 and 2 at% Zr at peak concentration in Si05 and Si18 alloy, respectively) is
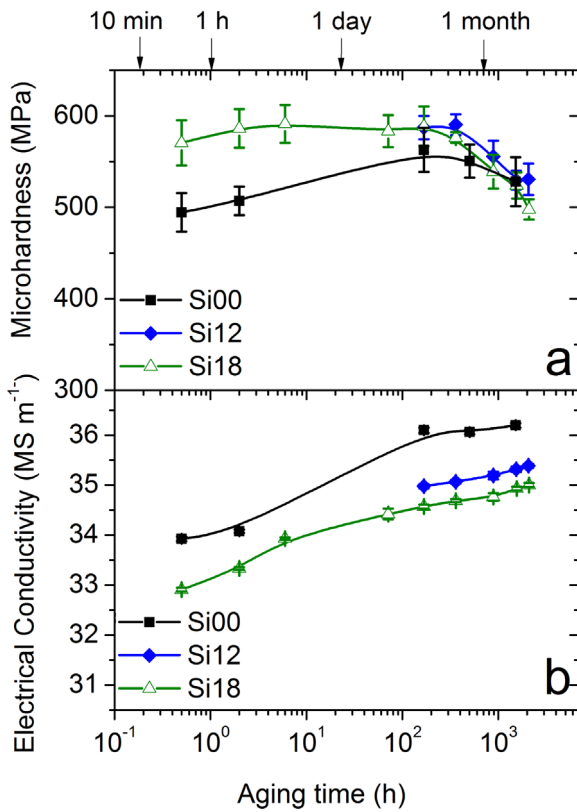
Fig. 6. Evolution of Vickers microhardness and electrical conductivity during iso-thermal aging at 375 °C after being homogenized at 640 °C for 72 h in the Si00 and for 2 h in the Si12 and Si18 alloys.
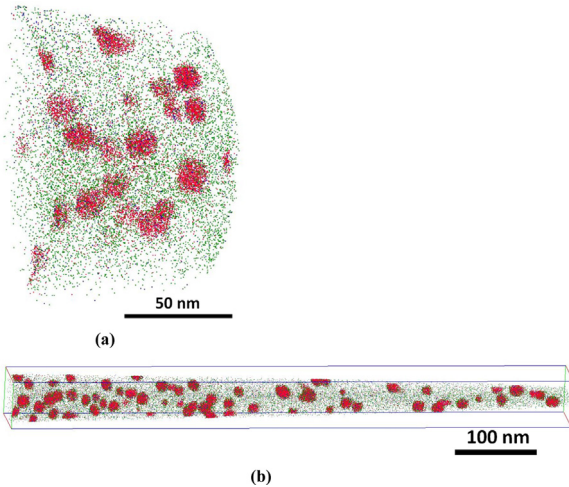

Fig. 7. Atom-probe tomographic reconstruction of the Si18 after 0.5 h (a) and 2 h (b) of aging, all isothermal at 400 °C, after being homogenized at 640 °C, showing nano-precipitates. Sc atoms are displayed in red, Zr atoms are in green, Er atoms are in blue, Si atoms are in black, and Al atoms are omitted for clarity. (For inter-pretation of the references to colour in this figure legend, the reader is referred to the web version of this article.)

surprising, because the $\sqrt{4Dt}$ value of Zr in pure Al [37] at 400 °C for 0.5 h is only 9 nm, which is significantly less than the estimated edge-to-edge inter-precipitate spacing of ∼70 nm (see Appendix A).

After 2 h of aging at 400 °C, the Si18 alloy exhibits precipitates at a number density of $1.90 \pm 0.27 \times 10^{22}$ m^{-3}, a mean radius of 3.1 ± 0.9 nm, and a volume fraction of 0.252%, Table 2. The average precipitate composition is 70.08 Al, 2.17 Zr, 21.04 Sc, 1.69 Er, and 5.02 Si at%, Table 3. Comparing to the same alloy composition after
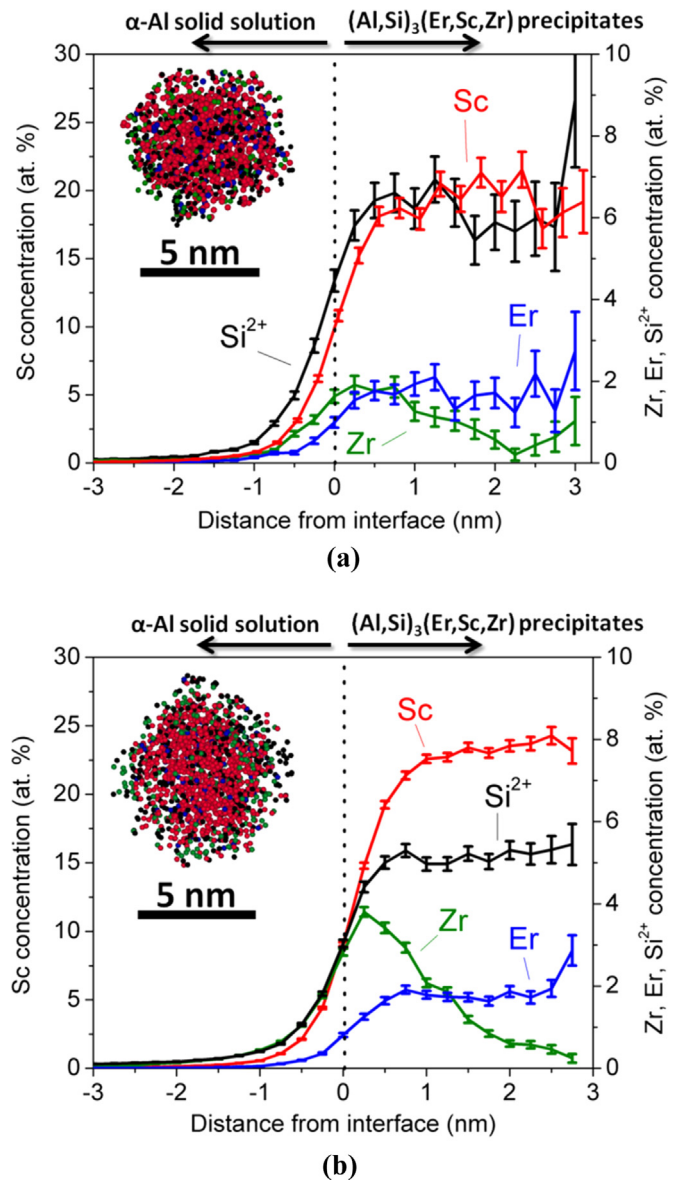

(a)

(b)

Fig. 8. Concentration profiles across the matrix/precipitate interface the Si18 after 0.5 h (a) and 2 h (b) of aging, all isothermal at 400 °C, after being homogenized at 640 °C. In inset image is the APT reconstruction of a representative precipitate from the alloy. Sc atoms are displayed in red, Zr atoms are in green, Er atoms are in blue, Si atoms are in black, and Al atoms are omitted for clarity. (For interpretation of the references to colour in this figure legend, the reader is referred to the web version of this article.)

Table 2

Precipitate number density, N_v, mean radius, $<R>$, volume fraction, ϕ, and mi-crohardness, HV, for studied alloys aged isothermally at 400 °C for different times, after being homogenized at 640 °C.

Alloys	N_v ($\times 10^{22}$ m^{-3})	$<R>$ (nm)	ϕ (%)	HV (MPa)
Si05 isothermal at 400 °C for 0.5 h [20]	1.11 ± 0.37	4.1 ± 0.8	0.235	504 ± 13
Si05 isothermal at 400 °C for 66 days [20]	0.20 ± 0.10	6.3 ± 0.3	0.210	429 ± 14
Si18 isothermal at 400 °C for 0.5 h	2.23 ± 0.57	2.9 ± 0.7	0.229	536 ± 16
Si18 isothermal at 400 °C for 2 h	1.94 ± 0.27	3.1 ± 0.9	0.252	607 ± 9

Table 3
Composition of precipitates and matrix in studied alloys aged isothermally at 400 °C for different times, after being homogenized at 640 °C.

Alloys	Precipitate composition (at%)					Matrix composition (at. ppm)			
	Al	Si[*]	Sc	Zr	Er	Si[*]	Sc	Zr	Er
Si05 isothermal at 400 °C (0.5 h) [20]	73.35(21)	2.75(8)	21.38(20)	0.30(3)	2.22(7)	274(3)	76(2)	157(3)	21(9)
Si05 isothermal at 400 °C (66 days) [20]	74.17(13)	1.13(3)	19.53(12)	3.46(6)	1.71(4)	441(7)	49(2)	14(1)	14(1)
Si18 isothermal at 400 °C (0.5 h)	74.52(27)	5.81(14)	16.72(23)	1.41(7)	1.54(8)	845(7)	63(2)	242(4)	4(1)
Si18 isothermal at 400 °C (2 h)	70.08(11)	5.02(5)	21.04(10)	2.17(4)	1.69(3)	902(8)	55(2)	72(2)	0(2)

[*] Atomic concentration of $^{28}Si^{2+}$ ions in LEAP.

0.5 h of aging, the precipitate number density is slightly smaller, from $2.23 \pm 0.57 \times 10^{22}$ to $1.94 \pm 0.27 \times 10^{22}$ m^{-3}, the mean radius is slightly larger, from 2.9 ± 0.7 to 3.1 ± 0.9 nm, while the volume fraction increases from 0.229% to 0.252%, Table 2. The precipitates also contain higher concentrations of Sc and Zr after 2 h of aging. The peak concentration of Zr in the Zr-enriched shell is ∼4 at%. These observations indicate that the Si18 alloy is still in the growth regime after 2 h of aging, consistent with an increase in microhardness from 0.5 to 2 h of aging.

To examine the role of Si in accelerating Zr precipitation, Zr concentration profiles in precipitates of the Si00 [21], Si05 [20], Si18 alloys after 0.5 h of aging at 400 °C are plotted in Fig. 9. It is apparent that the higher the Si concentration, the higher is the Zr peak concentration in the Zr-enriched shell of the precipitates: 0.3, 0.5, 2 at% in the Si00, Si05, and Si18 alloys, respectively. The root-mean-square diffusion distance ($\sqrt{4Dt}$) of Zr in pure Al [37] at 400 °C for 0.5 h is 9 nm, while the estimated edge-to-edge inter-precipitate spacing is ∼70 nm. This observation suggests that Zr solute diffuses faster in the presence of Si in the α-Al matrix, which may occur by formation of Si–Zr dimers, which diffuse faster than Zr monomers in the α-Al matrix by analogy with what was found for Si and Sc atoms in the α-Al matrix [22].

3.5.2. Later stage of isothermal aging at 400 °C

APT was utilized in our prior work to study the nanostructure of precipitates of the Si05 alloy, aged at 400 °C for 66 days, after being homogenized for 72 h [20]. The precipitate mean radius is 6.3 ± 0.3 nm, their number density is $0.20 \pm 0.10 \times 10^{22}$ m^{-3}, and their volume fraction is 0.210%. Comparing these results for the same alloy aged for 0.5 h, the precipitate number density decreases by a factor of four, while the mean radius increases by a factor 1.5 and the volume fraction remains relatively constant [20]. The coarsening nanostructure of the precipitates is apparent in the precipitate concentration profile. The precipitates consist of an inner core and outer shell with different compositions of Er, Si, and Zr. The inner core, with a 2–3 nm radius (and corresponding to 2–8 vol%), is the result of an initial nucleation and growth stage, and has a composition of 71.80 Al, 1.50 Zr, 22.11 Sc, 2.65 Er, and 1.63 at% Si. The outer shell, is the result of subsequent coarsening, which has a composition of 72.93 Al, 3.98 Zr, 20.11 Sc, 1.55 Er, and 1.01 Si at% [20].

Beyond 64 days of aging at 400 °C, the increment of microhardness (ΔHV) of the Si12 and Si18 alloy is small, > 100 MPa, as compared to the microhardness of the precipitate-free Al alloy, Fig. 4. Hence, a large precipitate mean radius (> 10 nm) and a low number density (< 10^{21} m^{-3}) is anticipated in these alloys, which are difficult to characterize by APT. For example, a precipitate number density of 10^{20} m^{-3} requires an APT analyzed volume of ∼3×10^8 atoms (∼10^7 nm^3) to observe a single precipitate, while the average analyzed volume only contains ∼5×10^7 atoms (∼1.5×10^6 nm^3) in Al alloys. While characterization can be achieved by analyzing numerous APT specimens of the same alloy to improve the counting statistics, it is, however, time-consuming and expensive. Therefore, the mean precipitate radius and number density in the Si18 alloy, isothermally aged at 400 °C for 64 day, were estimated to be 10–15 nm and
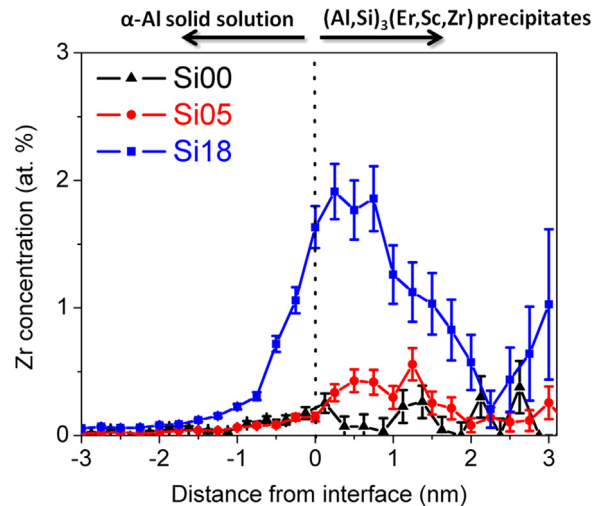

Fig. 9. Zr concentration profiles across the matrix/precipitate interface of the Si00 [21], Si05 [20], and Si18 after 0.5 h of isothermal aging at 400 °C, after being homogenized at 640 °C.

$0.3–1 \times 10^{21}$ m^{-3}, respectively, assuming the Er, Sc, and Zr atoms are fully precipitated and the Orowan looping strengthening mechanism is the only operative one at this stage, Fig. 10. These assumptions are proven to be valid for the Si05 alloy, which was aged isothermally at 400 °C for 66 day [20], Tables 3 and 4.

4. Discussion

4.1. Strengthening mechanisms

Possible precipitate strengthening mechanisms are given in the Appendix A, including coherency and modulus strengthening ($\sigma_{coh} + \sigma_{mod}$), ordering strengthening (σ_{ord}), and Orowan dislocation looping strengthening (σ_{Or}). The calculated yield strength increment of alloys due to aged precipitates, whose APT data are given in Table 4, are compared to the measured strength increment, estimated as $\Delta HV/3$ [28], where ΔHV is the microhardness increase from the base microhardness of 200 MPa of the precipitate-free Al alloy [28] to the microhardness in the aged state. For the Si05 alloy aged isothermally at 400 °C for 0.5 h and displaying a precipitate mean radius of 4.1 nm, the measured strength increment (101 ± 5 MPa) is slightly greater than for the calculated Orowan dislocation looping (89 MPa) mechanism, but smaller than the calculated ordering strengthening mechanism (114 MPa) [20]. The precipitate radius is in the critical range of 2.0–4.0 nm, where the controlling deformation mechanism changes from precipitate shearing to Orowan dislocation looping [56]. Thus, a mixed strengthening mechanism may be active, which was observed in prior works [42,43,55,56]. For the same alloy, but aged for 66 days and showing a larger average precipitate radius of 6.3 nm, the measured strengthing increment is 76 ± 5 MPa. This value is closest to the calculated Orowan dislocation looping strengthening mechanism

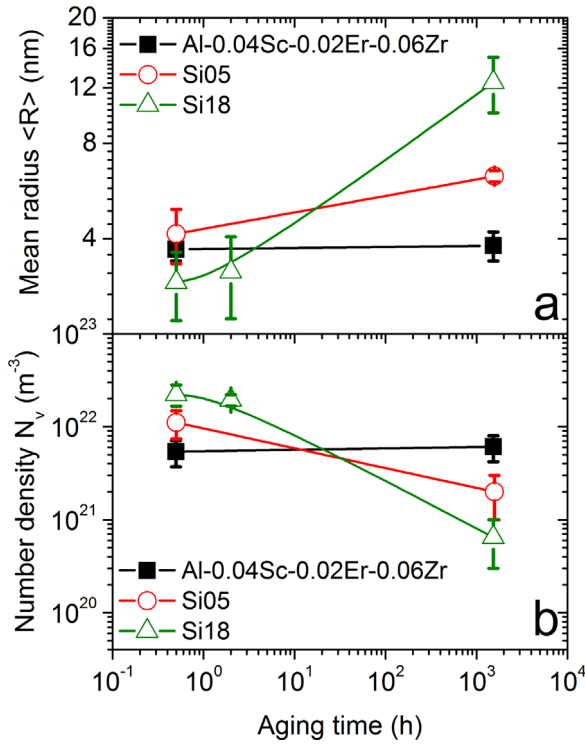**Fig. 10.** Evolution of precipitate mean radius, $<R>$, and number density, N_v, of the Al-0.04Sc-0.02Er-0.06Zr at% [21], Si05 [20], and Si18 alloys during isothermal aging at 400 °C, after being homogenized at 640 °C for 72 h in the two earlier alloys, and for 2 h in the latter alloy, obtained by APT, except for the data point of the Si18 at 1536 h, which was estimated.

(62 MPa). We, therefore, conclude that the Orowan bypass strengthening mechanism is operative in this alloy. In the Si18 alloy, aged for 0.5 and 2 h and with precipitate mean radii of 2.9 and 3.1 nm, respectively, the measured strengthening increments are 112 ± 5 and 136 ± 3 MPa, respectively. The latter value is higher than for both the calculated Orowan dislocation looping and ordering mechanisms, but much lower than the sum of coherency and modulus strengthening mechanisms. The earlier value is close to both calculated Orowan dislocation looping and ordering strengthening mechanisms. Thus, mixed strengthening mechanisms may be operative in both alloys.

4.2. Effects of silicon additions

4.2.1. Strengthening in the homogenized state of Si-containing alloys

Fig. 5 displays a monotonic relationship between the Si concentration and the microhardness of the alloys after homogenization. It is unexpected since all solutes are anticipated to be dissolved completely in the α-Al matrix after homogenization and quenching, and since hardening from the solid solution at this low total solute concentration is negligible [44]. A hardness increase of only 14 MPa is estimated from solid-solution hardening of 0.2 at% Si in an Al-Si binary alloy [45]. Thus, a microhardness increase of 71 ± 10 MPa in the Si18 alloy compared to the Si00 alloy in the homogenized state

must be due to another strengthening mechanism. Specifically, APT analyses reveal the formation of Si-enriched nanoclusters, containing trace concentrations of Er and Sc, in the homogenized Si18 alloy (not displayed). The clustering of Si atoms most likely occurs during rapid water quenching after homogenization, due to the high diffusivity of Si in α-Al, which is similar to Al self-diffusion [46], and due to the attractive binding energy between a Si atom and a vacancy [19]. It should be noted that there exists a possibility that Si atoms might cluster during atom evaporation in the APT experiment. New surfaces are created during this process, where Si atoms can rapidly diffuse and form clusters. Formation of divacancies also occurs during quenching [47–49], and they can accelerate solute diffusion kinetics in aluminum even at room temperature, where all studied samples were stored for a duration of a few days before the microhardness and APT experiments. Therefore, formation of Si atom clusters due to room temperature diffusion is also possible.

4.2.2. Acceleration of precipitation kinetics

Two signatures of the acceleration of precipitation kinetics, in the presence of Si, are revealed in the isothermal aging behavior at 400 °C. Firstly, the microhardness of the Si05 alloy increases rapidly from the homogenized state to achieve a high value of 500 MPa after only 0.1 h, while five times longer is required for the Si00 alloy to achieve 430 MPa. Secondly, alloys with higher Si concentrations show shorter peak-aging time: 380, 60, 2, and 2 h for the Si00, Si05, Si12, and Si18 alloys, respectively, Figs. 4 and 5. These experimental results further support the conclusions of first-principle calculations, demonstrating how Si accelerates Sc precipitation kinetics in the Al-0.06Sc-0.06Zr-0.06Si alloy aged at 300 °C [19]. The calculated solute-solute binding energies of a Si-Sc pair at the first and second nearest-neighbor (NN) distances are 0.33 and 0.13 eV pair^{-1}, respectively, which are attractive energies. Sc-Si pairs are also highly attractive to vacancies. A Sc-Si-vacancy trimer has a binding energy between -0.17 and 0.08 eV vacancy^{-1}; the exact value depends on the specific configuration of Sc, Si, and the vacancy in the lattice. While the Sc-vacancy binding energy, in the absence of Si, is -0.25 eV vacancy^{-1}, which is less attractive. Furthermore, the Sc migration energy is decreased from 0.74 eV atom^{-1} in the absence of Si, to 0.45 eV atom^{-1} in its presence, for a configuration that results in an attractive Si-Sc binding following a Sc-vacancy exchange [19]. In summary, Si appears to be a solute diffusion enhancer, by binding itself to a vacancy(s) and Sc solute in Al-Sc-Si alloys. A higher Si concentration in the α-Al matrix results in an enhanced acceleration of solute diffusion kinetics. Whether Si has the same effect on Er and Zr is unknown and should be studied in the Al-Er-Si and Al-Zr-Si alloys, respectively.

4.2.3. Heterogeneous nucleation by Si additions

During isothermal aging at 400 °C, the alloy peak-microhardness increases with Si concentration , Fig. 5: 463 ± 20, 533 ± 12, 571 ± 12, and 607 ± 9 MPa in the Si00, Si05, Si12, and Si18 alloys, respectively. With similar supersaturations of Sc, Zr, or Er, the addition of Si accelerates the Al$_3$(Zr, Sc, Er) precipitation kinetics. After 0.5 h of aging at 400 °C the precipitate number density in Al-0.04Sc-0.02Er-0.06Zr, which has a similar microhardness to the Si00 alloy [21], is $0.54 \pm 0.17 \times 10^{22}$ m^{-3}, with an average radius of

Table 4
Experimental (ΔHV/3) and calculated strength increments (Eqs. (1A)–(4A)) of the studied alloys aged isothermally at 400 °C for different times, after being homogenized at 640 °C.

Alloys	ΔHV/3 (MPa)	$\Delta\sigma_{ord}$ (MPa) (Eq. (1A))	$\Delta\sigma_{coh}+\Delta\sigma_{mod}$ (MPa) (Eqs. (2A) and (3A))	$\Delta\sigma_{Or}$ (MPa) (Eq. (4A))
Si05 isothermal at 400 °C for 0.5 h [20]	101 ± 5	114	186	89
Si05 isothermal at 400 °C for 66 days [20]	76 ± 5	108	204	62
Si18 isothermal at 400 °C for 0.5 h	112 ± 5	113	139	111
Si18 isothermal at 400 °C for 2 h	136 ± 3	118	161	112

3.7 ± 0.3 nm [21]. These values are $1.11 \pm 0.37 \times 10^{22}$ m^{-3} and 4.1 ± 0.8 nm, and $2.23 \pm 0.57 \times 10^{22}$ m^{-3} and 2.9 ± 0.7 nm for the Si05 and Si18 alloys, respectively. This comparison suggests that Si additions linearly increase the precipitate number density, which decreases concomitantly the edge-to-edge inter-precipitate distance, thus increasing the precipitate strengthening contribution due to Orowan dislocation looping. With an attractive binding energy between a Si atom and a vacancy [19], Section 4.2.1, Si-vacancy clusters created during quenching from the homogenization temperature could serve as heterogeneous nucleation centers for Al$_3$(Zr, Sc, Er) precipitates, which form during aging. A similar effect was reported in Al-Mg-Sc alloys, where Mg stimulates heterogeneous nucleation of Al$_3$Sc precipitates [50–52].

4.2.4. Reduction of coarsening resistance

Si additions also lead to a reduction in the coarsening resistance of Al$_3$(Zr, Sc, Er) precipitates. The microhardness evolution during isothermal aging at 400 °C, Figs. 4 and 5, displays an earlier decrease in microhardness in the alloy containing higher Si concentration. The microhardness decrease between 2 and 700 h of aging, Fig. 5, is linear with increasing concentration Si concentration. APT results for the Si05 alloy demonstrate that the precipitates' average radius increases from a value of 4.1–6.3 nm for 0.5 h to 66 day of aging [20]. In contrast for the Al-0.04Sc-0.02Er-0.06Zr alloy the average radius has a constant value of 3.7 nm for the same range of aging times [21].

For the Si18 alloy the average precipitate radius increases from 3 nm after aging for 0.5 h to estimated 18 nm after aging for 64 days at 400 °C. The high coarsening resistance, reported previously [21,23,24,51,53,54] is due to the formation of a Zr-enriched shell enveloping the precipitates, which is a diffusion barrier for solutes within the precipitate core [21,54,55]. A Si addition has two possible effects. Firstly, Si may enhance the diffusion kinetics of solutes through the Zr-enriched surrounding the precipitates, thereby reducing the effectiveness of the diffusion barrier. Secondly, Zr diffusion kinetics in the α-Al matrix may also be enhanced by a Si addition via the mechanism demonstrated for Sc in the α-Al matrix [19]. The role of Si in accelerating the diffusion kinetics of Zr in dilute Al-Zr binary alloys is deduced from the more rapid decrease in microhardness in the Al-Zr-Si alloy [8–10]. The two proposed mechanisms responsible a reduction in precipitate coarsening resistance should be studied utilizing first-principles calculations in future research.

4.2.5. Modification of precipitate concentration profile

The last effect of a Si addition is to modify the concentration profiles within precipitates, Figs. 8 and 10. Prior research on Al-Zr-Sc-Er alloys, aged isochronally or isothermally, demonstrates that Al$_3$(Zr, Sc, Er) precipitates always consist of three distinct components: (i) an Er-enriched core (ii) a Sc-enriched inner shell; and (iii) a Zr-enriched outer shell [21]. The formation of core-double-shell precipitates is a consequence of sequential precipitation of Er, Sc and Zr due to their disparate intrinsic diffusivities in the α-Al matrix "$D_{Er} < D_{Sc} < D_{Zr}$" [21]. Mobility of solutes within the L1$_2$-ordered structure is anticipated to be low, hence maintaining the concentration profile throughout the aging [21]. In all the present Si-containing alloys, however, precipitates consist of a homogenized mixture of Er, Sc, and Si in the core and a Zr-enriched shell, Fig. 8. Precipitates in the alloy containing higher Si concentration consist of a higher Si content within the core, ~3 and ~6 at% in the Si05 [20] and Si18 alloys, respectively, isothermally aged at 400 °C for 0.5 h. The modification of precipitate core chemical structure can be explained by two possible mechanisms. First, while Er diffuses faster than Sc in α-Al matrix [35], Sc-Si dimers might diffuse as fast as Er-Si dimers, resulting in the co-precipitation of the three elements during aging. Second, Sc and Er diffusion kinetics might

possibly be accelerated in the L1$_2$-ordered precipitates by existence of Si, removing the concentration gradients within them caused by sequential precipitation. The two proposed mechanisms responsible for the change in precipitate chemical structure could be validated by first-principles calculations in the future work.

5. Conclusions

The effects of various Si additions (0, 0.05, 0.12 and 0.18 at%, labeled Si00, Si05, Si12, and Si18, respectively) in a cast Al-0.055Sc-0.005Er-0.02Zr at% alloy were systematically investigated by microhardness measurement, electrical conductivity, scanning electron microscopy, and atom-probe tomography. The following conclusions are drawn:

Homogenization for at least 0.5 h at 640 °C is needed to eliminate Al$_3$Er primary precipitates, enhance grain growth (and thus minimize grain boundary creep at high temperature) and maximize the Er supersaturation in the α-Al matrix during subsequent aging (thus increasing the number density of precipitates).

Alloys containing higher Si concentration display shorter peak-aging time at 400 °C: 380, 60, 2, and 2 h for Si00, Si05, Si12, and Si18 alloys, respectively. This effect is consistent with diffusion of Sc atoms being accelerated when Si is present in the α-Al matrix, which is determined in prior work [19] utilizing first-principles calculation, where it was found that a vacancy is more likely to be in the vicinity of a Sc atom when it is bound to a Si atom. Moreover, the calculations show that Sc migration energy in Al is decreased when it bounds to a Si atom. Whether a similar effect occurs to Er atoms is unknown.

Alloys containing higher Si concentration achieve higher microhardness after peak-aging at 400 °C: 463 ± 20, 533 ± 12, 571 ± 12, and 607 ± 9 MPa in Si00, Si05, Si12, and Si18 alloys, respectively. The above prior work [19] utilizing first-principles calculation demonstrates an attractive binding energy between Si and a vacancy, Si-vacancy clusters might act as heterogeneous nucleation sites. Thus, addition of Si very likely causes heterogeneous nucleation of Al$_3$(Sc, Zr, Er) precipitates, which increases number density and decreases radius in the peak-aging condition. Based on the Orowan strengthening mechanism, this results in a higher mechanical strength.

After 0.5 h of aging at 400 °C, the Si05 alloy exhibits precipitates with a number density $N_v = 1.11 \pm 0.37 \times 10^{22}$ m^{-3}, average radius $<R> = 4.1 \pm 0.8$ nm, and volume fraction $\phi = 0.235\%$ [20]. At the same heat aging condition, the Si18 alloy shows $N_v = 2.23 \pm 0.57 \times 10^{22}$ m^{-3}, $<R> = 2.9 \pm 0.7$ nm, and $\phi = 0.229$. Both precipitate chemical structures display a homogenized mixture of Sc, Er, and Si, surrounded by a shell slightly enriched in Zr, more so in the Si18 alloy. After 66 d of aging at 400 °C, the Si05 alloy the precipitates have $N_v = 0.20 \pm 0.10 \times 10^{22}$ m^{-3}, $<R> = 6.3 \pm 0.3$ nm, and $\phi = 0.210$, with an inner core enriched in Sc, Er, and Si, and an outer shell enriched in Zr [20]. At the same heat aging condition, the Si18 alloy was estimated to have $N_v \sim 0.3$–1×10^{21} m^{-3} and $<R> \sim 10$–15 nm.

Si additions reduce, however, the coarsening resistance of precipitates. Alloys containing higher Si concentration exhibit an earlier decrease in the microhardness and a faster decrease rate compared to the Si00 alloy. During aging at 400 °C, precipitates coarsen from $<R> = 4.1$–6.3 nm and 2.9 to 10–15 nm when aged from 0.5 h to 66 days in the Si05 and Si18 alloys, respectively, while maintaining $<R> = 3.7$ nm after the same aging period in the Al-0.04Sc-0.02Er-0.06Zr alloy [21]. Two possible mechanisms are possible:

(a) Silicon accelerates diffusion of Sc and Er in the Zr-enriched outer shell.
(b) Silicon accelerates Zr diffusion kinetics within the α-Al matrix by the same mechanism that Si accelerates Sc diffusivity.

Addition of Si modifies the concentration profiles within precipitates, enhancing the chemical homogeneity of Sc and Er in the core, rather than forming Er-enriched-core/Sc-enriched-shell observed in prior work [21]. Two possible mechanisms are possible:

(a) Silicon promotes co-precipitation of Sc and Er to form $Al_3(Sc, Er)$ in α-Al matrix.
(b) Silicon accelerates the Sc and Er diffusion kinetics in the $L1_2$-ordered precipitates.

Acknowledgments

Appendix A

Precipitate strengthening results from order strengthening, coherency strengthening, modulus mismatch strengthening, and Orowan dislocation looping. Relationships for the yield strength increments from each of these contributions of Al_3Sc precipitate in α-Al matrix are from Refs. [21,56]. The order strengthening, $\Delta\sigma_{ord}$, is given by:

$$\Delta\sigma_{ord} = 0.81 M \frac{\gamma_{APB}}{2b}\left(\frac{3\pi\phi}{8}\right)^{1/2}.$$ (1A)

where $M=3.06$ is the mean matrix orientation factor for Al [57], b $=0.286$ nm is the magnitude of the matrix Burgers vector [43], ϕ is the volume fraction of precipitates, and $\gamma_{APB}=0.5\,J\,m^{-2}$ is an average value of the Al_3Sc anti-phase boundary (APB) energy for the (111) plane [58–60].

The coherency strengthening $\Delta\sigma_{coh}$ is given by:

$$\Delta\sigma_{coh} = M\alpha_{\varepsilon}(G\theta)^{3/2}\left(\frac{<R>\phi}{0.5Gb}\right)^{1/2};$$ (2A)

where $\alpha_{\varepsilon}=2.6$ is a constant [61], $<R>$ is the average precipitate radius, and $\theta=0.88\%$ [62] is the constrained lattice parameter mismatch at room temperature.

The modulus mismatch strengthening, $\Delta\sigma_{mod}$, is given by:

$$\Delta\sigma_{mod} = 0.0055M(\Delta G)^{\frac{3}{2}}\left(\frac{2\phi}{Gb^2}\right)^{\frac{1}{2}}b\left(\frac{<R>}{b}\right)^{\left(\frac{3m}{2}-1\right)};$$ (3A)

where $\Delta G=42.5$ GPa is the shear modulus mismatch between the matrix and the Al_3Sc precipitates [63], and m is a constant taken to be 0.85 [61].

Finally, strengthening due to Orowan dislocation looping $\Delta\sigma_{Or}$ is given by:

$$\Delta\sigma_{Or} = M\frac{0.4}{\pi}\frac{Gb}{\sqrt{1-\vartheta}}\frac{\ln\left(\frac{2(\sqrt{\frac{2}{3}}<R>)}{b}\right)}{\lambda};$$ (4A)

where $\nu=0.34$ is Poisson's ratio for Al [57]. The edge-to-edge inter-precipitate distance, λ, is taken to be the square lattice spacing in parallel planes, which is given by [64]:

$$\lambda = \left[\left(\frac{3\pi}{4\phi}\right)^{\frac{1}{2}}-1.64\right]<R>$$ (5A)

References

[1] V.G. Davydov, T.D. Rostova, V.V. Zakharov, Y.A. Filatov, V.I. Yelagin, Mater. Sci. Eng. A 280 (2000) 30.
[2] V.V. Zakharov, Met. Sci. Heat Treat. 39 (1997) 61.
[3] V.V. Zakharov, T.D. Rostova, Met. Sci. Heat Treat. 49 (2007) 435.
[4] M.L. Kharakterova, D.G. Eskin, L.S. Toropova, Acta Met. 42 (1994) 2285.
[5] L.L. Rokhlin, T.V. Dobhatkina, M.L. Kharakterova, Powder Metall. Met. Ceram. 36 (1997) 128.
[6] O. Beeri, D.C. Dunand, D.N. Seidman, Mater. Sci. Eng. A 527 (2010) 3501.
[7] P. Malek, M. Janecek, B. Smola, Met. Mater. 38 (2000) 160.
[8] T. Ohashi, R. Ichikawa, J. Jpn. Inst. Met. 34 (1970) 604–610.
[9] T. Sato, A. Kamio, G.W. Lorimer, Mater. Sci. Forum 217–222 (1996) 895–900.
[10] S. Hori, T. Kondo, S. Ikeno, J. Jpn. Inst. Light Met. 28 (1978) 79–84.
[11] D. Mitlin, V. Radmilovic, J.W. Morris Jr, Metall. Mater. Trans. A 31 (2000) 2697–2711.
[12] A.J. Perry, K.M. Entwistle, Philos. Magn. 18 (1968) 1085–1088.
[13] S. Hori, N. Furushiro, W. Fujitani, J. Jpn. Inst. Light Met. 31 (1981) 649–654.
[14] C. Wolverton, Acta Mater. 55 (2007) 5867–5872.
[15] D. Simonovic, M.H.F. Sluiter, Phys. Rev. B 79 (2009) 054304.
[16] G. Du, J. Deng, Y. Wang, D. Yan, L. Rong, Scr. Mater. 61 (2009) 532–535.
[17] J. Røyset, H. Hovland, N. Ryum, Mater. Sci. Forum 396–402 (2002) 619–624.
[18] M.J. Stowell, Mater. Sci. Technol. 18 (2002) 139–144.
[19] C. Booth-Morrison, Z. Mao, M. Diaz, D.C. Dunand, C. Wolverton, D.N. Seidman, Acta Mater. 60 (2012) 4740–4752.
[20] N.Q. Vo, D.C. Dunand, D.N. Seidman, Acta Mater. 63 (2014) 73–85.
[21] C. Booth-Morrison, D.C. Dunand, D.N. Seidman, Acta Mater. 59 (2011) 7029–7042.
[22] C. Booth-Morrison, D.N. Seidman, D.C. Dunand, Acta Mater. 60 (2012) 3643–3654.
[23] C.B. Fuller, J.L. Murray, D.N. Seidman, Acta Mater. 53 (2005) 5401.
[24] C.B. Fuller, D.N. Seidman, Acta Mater. 53 (2005) 5415.
[25] M.E. van Dalen, D.C. Dunand, D.N. Seidman, Acta Mater. 59 (2011) 5224.
[26] C.B. Fuller, D.N. Seidman, D.C. Dunand, Scr. Mater. 40 (1999) 691.
[27] R.A. Karnesky, D.N. Seidman, D.C. Dunand, Mater. Sci. Forum 519–521 (2006) 1035.
[28] M.E. Krug, Microstructural Evolution and Mechanical Properties in Al-Sc Alloys with Li and Rare Earth Additions (Ph.D. dissertation), Northwestern University, 2011.
[29] B.W. Krakauer, J.G. Hu, S.M. Kuo, R.L. Mallick, A. Seki, D.N. Seidman, J.P. Baker, R. Loyd, Rev. Sci. Instrum. 61 (1990) 3390–3398.
[30] B.W. Krakauer, D.N. Seidman, Rev. Sci. Instrum. 63 (1992) 4071–4079.
[31] D.N. Seidman, Annu. Rev. Mater. Res. 37 (2007) 127.
[32] T.F. Kelly, M.K. Miller, Rev. Sci. Instrum. 78 (2007) 031101.
[33] D.N. Seidman, K. Stiller, MRS Bull. 34 (2009) 717.
[34] L.G. Parratt, Probability and Experimental Errors in Science, John Wiley, New York, 1966.
[35] M.E. van Dalen, R.A. Karnesky, J.R. Cabotaje, D.C. Dunand, D.N. Seidman, Acta Mater. 57 (2009) 4081–4089.
[36] J.L. Murray, A.J. McAlister, The Al-Si (aluminum-silicon) system, Bull. Alloy Phase Diagr. 5 (1984) 74.
[37] T. Marumo, S. Fujikawa, K. Hirono, J. Jpn. Inst. Light Met. 23 (1973) 17.
[38] A.T. Macrander, M. Yamamoto, D.N. Seidman, S.S. Brenner, Rev. Sci. Instrum. 54 (1983) 1077.
[39] O.C. Hellman, J.A. Vandenbroucke, J. Rusing, D. Isheim, D.N. Seidman, Microsc. Microanal. 6 (2000) 437.
[40] O. Hellman, J. Vandenbroucke, J.B. du Rivage, D.N. Seidman, Mater. Sci. Eng. A 327 (2002) 29.
[41] O. Hellman, J.B. du Rivage, D.N. Seidman, Ultramicroscopy 95 (2003) 199.
[42] K.E. Krug, A. Werber, D.C. Dunand, D.N. Seidman, Acta Mater. 58 (2010) 134.
[43] M.E. van Dalen, D.C. Dunand, D.N. Seidman, J. Mater. Sci. 41 (2006) 7814.
[44] R.L. Fleisher, Solid solution hardening, in: D.M. Peckner (ed.), The Strengthening of Metals, Reinhold, NY, 1964.
[45] G.P.M. Leyson, W.A. Curtin, L.G. Hector Jr, C.F. Woodward Nat. Mater. 9 (2010) 750.
[46] S. Fujikawa, K. Hirano, Y. Fukushima, Metall. Trans. A 9 (1978) 1811.
[47] J.S. Koehler, F. Seitz, J.E. Bauerle, Phys. Rev. 107 (1957) 1499.

[48] M. Doyama, J.S. Koehler, Phys. Rev. 127 (1962) 21.
[49] H. Kimura, R. Maddin, D. Kuhlmann-Wilsdorf, Acta Met. 7 (1959) 145.
[50] E.A. Marquis, D.N. Seidman, Surf. Interface Anal. 36 (2004) 559.
[51] E.A. Marquis, D.N. Seidman, M. Asta, C. Woodward, Acta Mater. 54 (2006) 119.
[52] N.Q. Vo, D.C. Dunand, D.N. Seidman, Acta Mater. 60 (2012) 7078.
[53] V.G. Davydov, V.I. Elagin, V.V. Zakharov, T.D. Rostova, Metalloved. Term. Obrab. Met. 8 (1996) 25.
[54] K.E. Knipling, R.A. Karnesky, C.P. Lee, D.C. Dunand, D.N. Seidman, Acta Mater. 58 (2010) 5184.
[55] K.E. Knipling, D.N. Seidman, D.C. Dunand, Acta Mater. 59 (2011) 943.
[56] D.N. Seidman, E.A. Marquis, D.C. Dunand, Acta Mater. 50 (2002) 4021.
[57] M. Meyers, K. Chawla, Mechanical metallurgy: principles and applications, Englewood Cliffs, Prentice Hall, NJ, 1984.
[58] C. Fu, J. Mater. Res. 5 (1990) 971.
[59] E. George, D. Pope, C. Fu, J. Schneibel, ISIJ Int. 31 (1991) 1063.
[60] K. Fukunaga, T. Shouji, Y. Miura, Mater. Sci. Eng. A 239 (1997) 202.
[61] A.J. Ardell, Metall. Mater. Trans. A 16 (1985) 2131.
[62] K.E. Knipling, D.C. Dunand, D.N. Seidman, Z. fur Met. 97 (2006) 246.
[63] R.W. Hyland, R.C. Stiffler, Scr. Met. Mater. 25 (1991) 473.
[64] E. Nembach, Particle Strengthening of Metals and Alloys, John Wiley, New York, NY, 1997.